



Microstructural engineering of a dual-phase Ti-Al-V-Fe alloy via in situ alloying during laser powder bed fusion

Ming Chen^{a,1}, Steven Van Petegem^{a,*}, Zhiyi Zou^b, Marco Simonelli^b, Yau Yau Tse^c, Cynthia Sin Ting Chang^d, Malgorzata Grazyna Makowska^{a,2}, Dario Ferreira Sanchez^e, Helena Moens-Van Swygenhoven^a

^a Photons for Engineering and Manufacturing, Paul Scherrer Institut, Forschungsstrasse 111, 5232 Villigen PSI, Switzerland

^b Centre for Additive Manufacturing, University of Nottingham, UK

^c Department of Materials, Loughborough University, UK

^d ANAXAM, Technology Transfer Centre for Advanced Manufacturing, PARK INNOVAARE: deliveryLAB, 5234 Villigen PSI, Switzerland

^e MicroXAS Beamline, Paul Scherrer Institut, Forschungsstrasse 111, 5232 Villigen PSI, Switzerland

ARTICLE INFO

Keywords:

Laser powder bed fusion
Operando X-ray diffraction
In situ alloying
Ti-Al-V-Fe
Mechanical properties

ABSTRACT

When Ti-6Al-4V is processed by laser powder bed fusion (L-PBF), acicular martensitic α' -Ti grains are formed within the columnar prior β -Ti grains, resulting in inferior mechanical properties. The application of blended powders in L-PBF enables to tailor the microstructures and obtain a mixture of $\alpha' + \beta$ phases. In this work, we demonstrate an effective method to engineer the phase fraction of an L-PBF manufactured Ti alloy using blended powders consisting of Ti-6Al-4V and 3 wt% Fe particles. By varying laser parameters, the as-built microstructures transit from α' dominated microstructure to a nearly complete β -dominant microstructure. High-speed *operando* X-ray diffraction during L-PBF processing combined with X-ray fluorescence and EBSD characterization allows for relating microstructure to the spatial distribution of the β -stabilizer Fe under the high cooling rates typical for L-PBF. The as-built microstructure containing large amounts of β phase achieves high strength and enhanced ductility without post-processing heat treatments.

1. Introduction

Additive Manufacturing (AM) of metallic powders to build near-net-shaped components with complex structures has advanced in the last decade rapidly. Titanium (Ti) alloys, in particular Ti-6Al-4V (Ti64), with outstanding weldability, fabricated by Laser Powder Bed Fusion (L-PBF), have drawn enormous attention due to the high strength-to-weight ratio and excellent corrosion resistance for applications in aerospace and biomedical sectors. The continuous development of additively manufactured Ti alloys to foster their industrial adoption relies on achieving properties superior to the counterparts fabricated by conventional methods, like casting or forging. However, Ti64 fabricated by L-PBF suffers from the formation of hierarchical structures of acicular martensitic α' grains within large columnar of prior β grains [1]. This anisotropic microstructure with brittle martensitic phase results in inferior ductility, fatigue resistance and fracture toughness [2–5].

Significant efforts have been devoted to engineering the microstructures and phase fractions to improve mechanical properties. By varying laser parameters and scanning strategies, the complete martensitic structure can be decomposed into a mixture of brittle α and ductile β phases [6–8] by reducing cooling rates [9] or adding β -stabilizers [10]. For instance, it has been shown that the β phase can be partially retained in Ti64 by achieving low cooling rates (below 2.9×10^3 – 3.6×10^3 K/s) via the decrease of the laser scanning speed down to 0.03 m/s, much lower than the common values used in L-PBF process [9]. Post heat treatments with controlled thermal profiles allow to generate different phase fractions in the printed parts, and to some extent modify the morphologies of acicular α' grains to improve ductility and work hardening [11–13]. Meanwhile, an alternative method using blended powders containing β -stabilizers instead of pre-alloyed powders is emerging to manufacture Ti alloys with various microstructures and phase fractions via more sustainable in situ alloying methods during the L-PBF process [14–18].

* Corresponding author.

E-mail address: steven.vanpetegem@psi.ch (S. Van Petegem).

¹ Current address: Structure and Mechanics of Advanced Materials, Paul Scherrer Institute, Forschungsstrasse 111, CH-5232 Villigen PSI, Switzerland.

² Current address: MicroXAS Beamline, Paul Scherrer Institut, Forschungsstrasse 111, 5232 Villigen PSI, Switzerland.

The printed parts exhibit a wide range of mechanical properties for various applications, for instance, the high strength and ductility for aerospace components [19] and the low stiffness and superior fracture toughness for bone implants [20].

The application of blended powders feedstock L-PBF offers considerable freedom to design novel Ti alloys and sufficient flexibility to adjust their compositions. In addition, the mixed powders also lower the cost of powder manufacturing in contrast to the pre-alloyed powders. Various β -stabilizers have been added into Ti64-based powder mixtures to stabilize the metastable β phase, suppress the columnar shape of β grains and refine grain sizes simultaneously [21–24]. Adding 10–15 wt % Mo particles has shown to stabilize the β phase [25] and also suppresses columnar growth of β grains by promoting the transition from planar to cellular solidification [21]. However, the presence of retained hard Mo particles is detrimental to fatigue resistance. In addition, the high cost of Mo also restricts the wide adoption of such β -Ti alloys [26]. Cu particles improve the anti-bacterial properties of printed Ti alloys for hard tissue implants but also may lead to the unfavorable intermetallic CuTi_2 [22]. Rare and precious metals, such as Nb, Ta and Zr, have been used to reduce the modulus of printed Ti alloys for bone implants [23]. The addition of 3 wt% cost-effective Fe particles showed a great potential to fabricate metastable β -Ti alloys with refined β grains [24]. Fe exhibits a high growth restriction factor and diffusion coefficient in Ti alloys, which induces constitutional undercooling and promotes columnar to equiaxed transition (CET) during solidification [19,24,27–29]. Recently, Zhang et al. achieved a fine mixture of $\alpha' + \beta$ phase by mixing Ti64 with 316L, thereby inducing a local concentration modulation. This resulted in improved strength and ductility [29]. Most reports in the literature focus on the chemical composition of the powder mixtures and their effect on the phase fractions. But the elemental distribution plays an important role on microstructures and associated mechanical properties. For instance, it was shown that multiple thermal cycles are needed to homogenize the chemical composition of a high-Fe

β -Ti thin wall [30]. In other mixed powders containing Ti and different β -stabilizers (Cr, Nb, Mo, etc), the density, microstructures and hardness of printed parts were modified by controlling laser energy inputs and thermal profiles [31,32]. However, the correlation between the laser manufacturing parameters with the as-built microstructures using blended powders is still rarely explored for Fe modified Ti64 alloys.

In this study, we reveal the role of the L-PBF laser process parameters on the resulting microstructures and mechanical properties of a blended powder that consists of Ti64 with 3 wt% Fe particles. With increasing volume energy densities, the as-built microstructures transit from the β dominant to nearly complete α' microstructures. Superior mechanical properties are achieved in the β -dominant Ti-alloy. This study demonstrates an effective way to engineer specific microstructures and paves the way to create functionally gradient properties in additively manufactured Ti alloys by simply controlling laser manufacturing parameters.

2. Materials and methods

The base powder used in this study was provided by LPW Technology (now Carpenter Additive, USA). It is a pre-alloyed Ti-6Al-4V (Ti64) powder, produced by plasma atomization. The powder particles have a spherical morphology and exhibit the following size distribution: $D_{10} = 21.8 \mu\text{m}$, $D_{50} = 33 \mu\text{m}$ and $D_{90} = 49.5 \mu\text{m}$. A quaternary feedstock, denominated as Ti643, was prepared by decorating the Ti64 base powder with 3 wt% of Fe particles with 99.9 % purity (Goodfellow Cambridge Limited) by mixing Ti64 and Fe particles in a roller mixer for 1 hr. The fine Fe particles had a size distribution $D_{10} = 2.88 \mu\text{m}$, $D_{50} = 5.94 \mu\text{m}$, and $D_{90} = 12.4 \mu\text{m}$. Fig. 1a and b show back-scattered electron (BSE) micrographs of the Ti643 powder feedstock. The particle size distributions of pre-alloyed Ti64 and Fe measured by a Mastersizer 3000 (Malvern Panalytical) are plotted in Fig. 1c.

For the *operando* X-ray diffraction experiments, Ti643 cuboidal samples with a size of $6 \times 6 \times 2 \text{ mm}^3$ were printed on a Ti64 baseplate

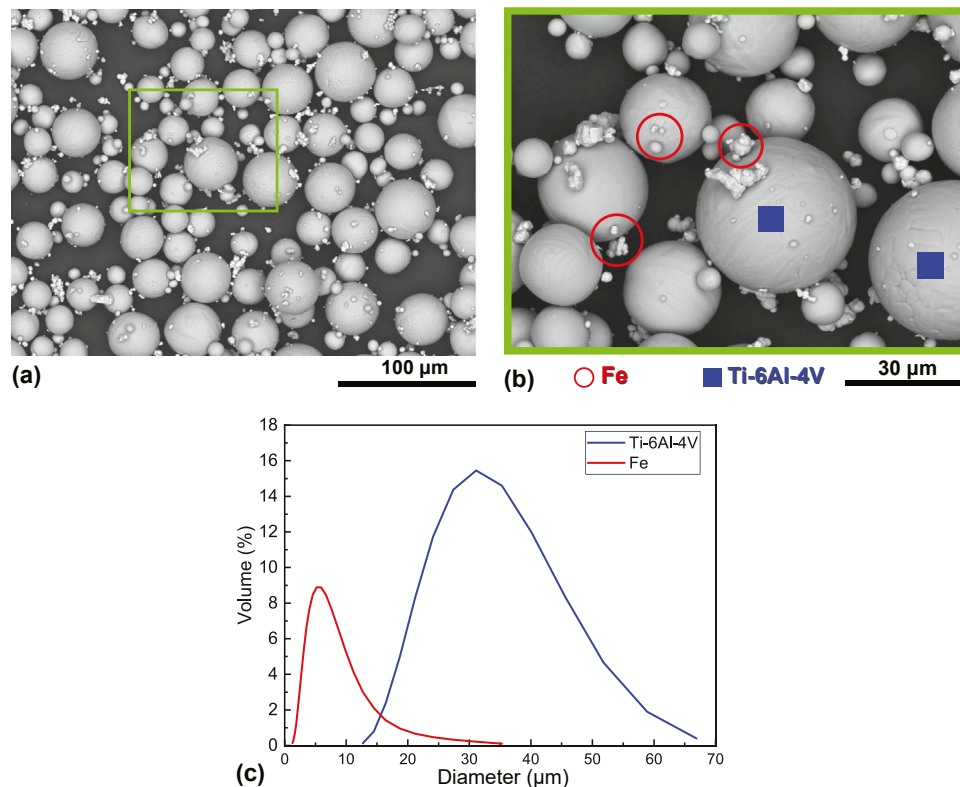


Fig. 1. Back-scattered electron micrograph (a) and magnified view (b) of the Ti643 powder feedstock as a mixture of pre-alloyed Ti64 (indicated by blue markers) and elementary Fe (circled in red). (c) Particle size distribution of Ti64 and Fe particles.

with a miniaturized L-PBF printer. Details on this setup can be found in Refs. [33,34]. During printing, the process chamber was continuously flushed with high purity Ar, to keep the oxygen levels well below 0.2 %. The laser power and scanning speed were varied to achieve different volume energy densities (VED) of 43 (S1), 85 (S2) and 107 (S3) J/mm³ in different specimens. The most critical laser process parameters for each specimen are summarized in Table 1. The laser focus diameter of miniaturized L-PBF printer is 50 μ m. A bidirectional scanning strategy was applied with 90 degrees rotation between each layer. The build plate of the miniaturized L-PBF printer for *operando* X-ray diffraction experiments has a small surface area of 12 \times 12 mm². Therefore, samples for tensile testing were printed separately in a commercial Renishaw AM400 L-PBF system which features a much larger build plate. Low VED and high VED parameters were optimized respectively to print nearly full dense material, with microstructures similar to what was obtained in the miniaturized printer. The laser processing parameters for tensile samples S4 and S5 are also listed in Table 1. The laser focus diameter is 75 μ m for tensile samples. Tensile specimens with a diameter of 4 mm and a gauge length of 20.4 mm were then machined from the center of the printed material, according to standard ASTM E8/E8M-16a. Room temperature tensile tests were conducted on an Instron 5969 at a displacement rate of 0.14 mm/min, with the test direction parallel to the build-direction (z-axis) of the printed material.

The *operando* X-ray diffraction experiments were performed on the MicroXAS beamline located at the Swiss Light Source. The X-ray beam had an energy of 12 keV and a full-width at half-maximum (FWHM) spot size of 45 \times 15 μ m² (width \times height). The printer was tilted by 18 degrees towards the direction of the incident X-ray beam, resulting in a projected area of 45 \times 46 μ m² (A_{XR}) illuminated by the X-ray beam. The X-ray beam is positioned at 1 mm from the outer edge of the printed area. A fast EIGER 1 M detector [35] recorded 2D diffraction patterns in reflection mode at a frame rate of 20 kHz and 45 μ s frame exposure time for a total duration of 1 s. The 2D diffraction images are reduced to conventional 1D diffraction patterns by azimuthal integration using pyFAI, an established python library for fast powder integration [36]. Before and after printing spatially resolved high-statistics diffraction patterns are recorded over an area of 6 \times 1.5 mm² with a step size of 0.1 mm.

The printed microstructures were analyzed by Scanning Electron Microscopy (SEM), Quanta 200 FEG, Thermo Fisher. The specimens were cut in half and then cold mounted with a conductive resin (Demotec 70, USA). The cross-section of the specimens was firstly mechanically polished using 6 μ m diamond suspension and up to 0.04 μ m colloidal silica to obtain a smooth surface. After that, the surfaces were etched with Kroll's reagent for 15–20 s. The microstructure and crystallographic phases were investigated by electron backscatter diffraction (EBSD) using a field emission gun operated at 25 keV in the SEM equipped with an EDAX Hikari Camera. The elemental distribution was simultaneously measured by energy-dispersive X-ray spectroscopy EDS (Octane Elite Super detector, EDAX, Inc., Mahwah, NJ, USA). The EBSD and EDS mappings were simultaneously performed with a step size of 200 nm. EDS point measurements of the local elemental composition were performed separately at a specimen tilting angle of 0 degrees. Post-processing of data and map reconstructions were done with the EDAX

OIM Analysis 7.3 software package.

3. Results

3.1. Operando X-ray diffraction

L-PBF manufacturing with blended powders is distinct from conventional printing with pre-alloyed powders since the phase transformation and resulting microstructures are profoundly affected by the interaction between mixed powders during fusion. To understand the phase evolution during L-PBF, *operando* X-ray diffraction was performed on specimens printed with different laser parameters as per Table 1. Fig. 2a–c display representative intensity versus diffraction and time waterfall plots during printing of multiple tracks in a single layer for samples S1–S3. Before printing, only the α/α' phase of Ti64 powders is detected. Diffraction peaks correlated with α -Fe are found at higher angles (see Fig. 2d). When the laser approaches A_{XR} , the blended powders first melt and then solidify to form the high-temperature β phase. This is observed as a break in the reflection lines of the α/α' phase because of the liquid phase in melt pool. Subsequently, the β reflections are detected after solidification, for instance for track 1 labeled in Fig. 2. When the laser moves away from A_{XR} , the β phase cools down and the reflection peaks shift to higher angles due to lattice contraction. At sufficiently low temperature, the α/α' phase reappears. Since multiple neighboring tracks are printed continuously on the same layer, the alternation between the α/α' and β phase at A_{XR} is repeated several times. When the distance between the laser track and A_{XR} is sufficiently large, the temperature in A_{XR} does not rise anymore above the β -transus temperature.

The evolution of XRD patterns in specimen S1 (Fig. 2a) shows a continuous line of $\{011\}\beta$ reflection during printing of multiple tracks, indicating the stabilization of the β phase after cooling in each track. In contrast, the $\{011\}\beta$ reflection in S2 (Fig. 2b) and S3 (Fig. 2c) nearly completely disappears when the laser moves away from A_{XR} between each track. This implies that the β phase in samples S2 and S3 is hardly stabilized after cooling down. Fig. 2d shows the diffraction intensity for a limited 2θ range obtained from spatially resolved XRD mapping on the surfaces of three specimens after printing. The XRD pattern for each specimen was obtained by summing up 50 individual patterns to improve grain statistics. Sample S1 exhibits a clear dual-phase structure consisting of a substantial fraction of β phase and a lower fraction of α/α' phase. In contrast, in samples S2 and S3 the α/α' phase is dominant. A weak $\{011\}\alpha$ -Fe peak is also detected after printing due to the redeposition of Fe particles on the sample surfaces. No evidence for intermetallic compounds, such as FeTi, could be found.

The XRD patterns from the *operando* measurements were further analyzed to evaluate the thermal profiles. The elastic strain of the crystalline lattice is determined by the relative shift of the peak positions (2 θ). Assuming that the peak shift during heating and cooling is entirely due to isotropic thermal expansion, temperatures of the solid phases can be derived [37]. In sample S1, the peak position of the $\{01-11\}$ α/α' reflection prior to printing was used as the reference value to calculate the temperature of the α/α' phase. Since the β phase is stabilized to ambient temperature, the peak position of $\{011\}\beta$ reflection after printing was applied to calculate temperatures of the β phase. For samples S2 and S3, the peak position of the $\{01-11\}\alpha'$ reflection after printing was used as a reference value. For the β phase, the same reference as in S1 was used. Fig. 3a–c show a zoom-in of the temperature-time profiles for S1–S3. The complete temperature profiles of three specimens can be found in Supplementary materials Fig. S1. In sample S1, the reference β transus temperature ($T_{\beta} \sim 1252$ K) of Ti64 [38] is only exceeded in two successive tracks. In contrast, the temperatures in samples S2 and S3, which were printed with higher VED, rise above T_{β} in neighboring 4 tracks. Note that the β transus ($T_{\beta} \sim 1252$ K), martensitic start ($M_s \sim 1053$ K) and martensitic finish ($M_f \sim 923$ K) of Ti64 [38] are shown as reference values only. The

Table 1
Overview of the laser process parameters for all samples.

Specimen number	Laser power (W)	Scan speed (m/s)	Layer thickness (μ m)	Hatch (μ m)	Volume energy density (J/mm ³)
S1	100	1.2	30	65	43
S2	100	0.6	30	65	85
S3	125	0.6	30	65	107
S4	150	1.62	30	65	47
S5	150	0.81	30	65	94

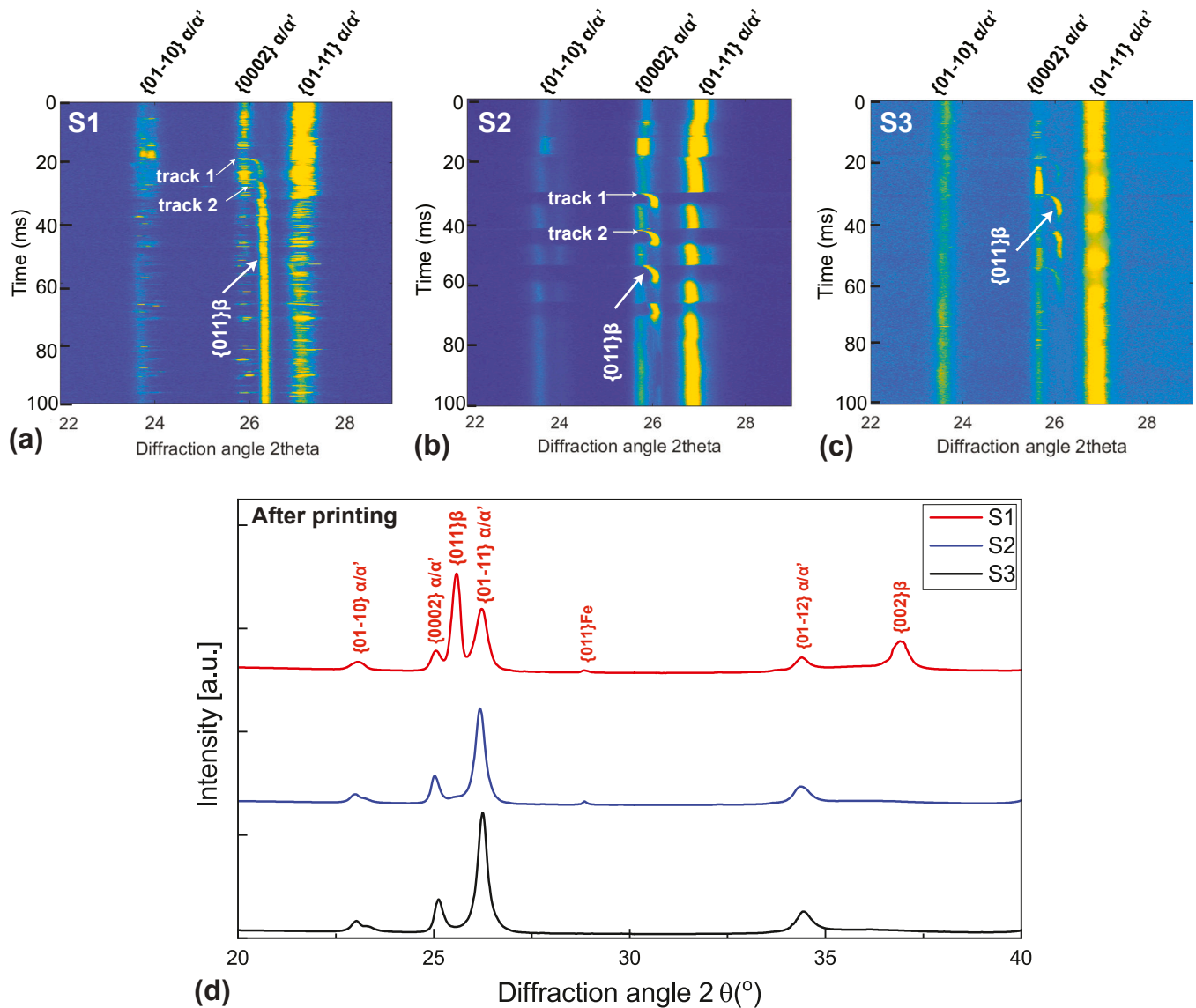


Fig. 2. Synchrotron X-ray diffraction (XRD) during and after printing: (a-c) Evolution of XRD patterns as a function of time measured by the X-ray beam on the surface layer during laser scanning. The color scale is cut at 0.5 counts per pixel to optimize visibility. As the samples were printed with different scanning speeds, the time axis was offset for easy comparison between the samples. (d) XRD patterns after laser printing in three specimens.

β -stabilizer Fe suppresses the $\beta \rightarrow \alpha/\alpha'$ transition and decreases phase transformation temperatures in Ti64 [39]. The effective transition temperatures in blended powders, therefore, depend on the locally chemical compositions [40]. But precise values of the transition temperatures are difficult to estimate in the printed Ti643 samples due to the chemical heterogeneity.

The cooling rates are determined as the derivatives of the temperature-time profile for different tracks, using the procedure described in Ref. [42] and the [Supplementary materials Section 5](#). [Fig. 3d](#) displays the cooling rates as a function of temperature for two successive tracks of samples S1–S3. The average cooling rates at T_p , M_s and M_f calculated from multiple tracks are plotted as a function of VED in [Fig. 3e](#). The cooling rates in sample S1 are 5–7 times higher than S2 and S3 at the same critical temperatures. It is important to note that the temperature calculation during in situ alloying is only approximate. A list of potential sources of errors is provided in [Supplementary Materials Section 6](#).

3.2. Microstructure characterization

[Fig. 4a–c](#) show backscattered electron micrographs of samples S1–S3 after etching. The β grain boundaries were observed in all samples after etching with Kroll's reagent. The β grain size is much finer in S1 compared to S2 and S3. Moreover, the acicular martensite is extensively distributed in the prior- β grains in both S2 and S3, a typical microstructure observed in Ti64 from the L-PBF process [43]. But this is not the case in S1 printed with relatively low VED. In addition, the melt pool in S1 with a depth of about $\sim 30 \mu\text{m}$ is much shallower compared to samples S2 and S3, with depths of $\sim 90\text{--}100 \mu\text{m}$, i.e. roughly three layers. This result indicates a transition from a conductive mode in S1 to a keyhole mode in S2 and S3 by increasing energy inputs [44]. Small pores induced by the unstable motion of keyhole tips under the keyhole mode are also found in S3 ([Fig. 4c](#)) [44].

To further characterize the grain structures for different phases, EBSD measurements were conducted in samples S1 and S2. The inverse pole figure (IPF) orientation map for sample S1 ([Fig. 4d](#)) exhibits a microstructure that mainly consists of fine β grains. This grain refinement results from the constitutional undercooling brought by the

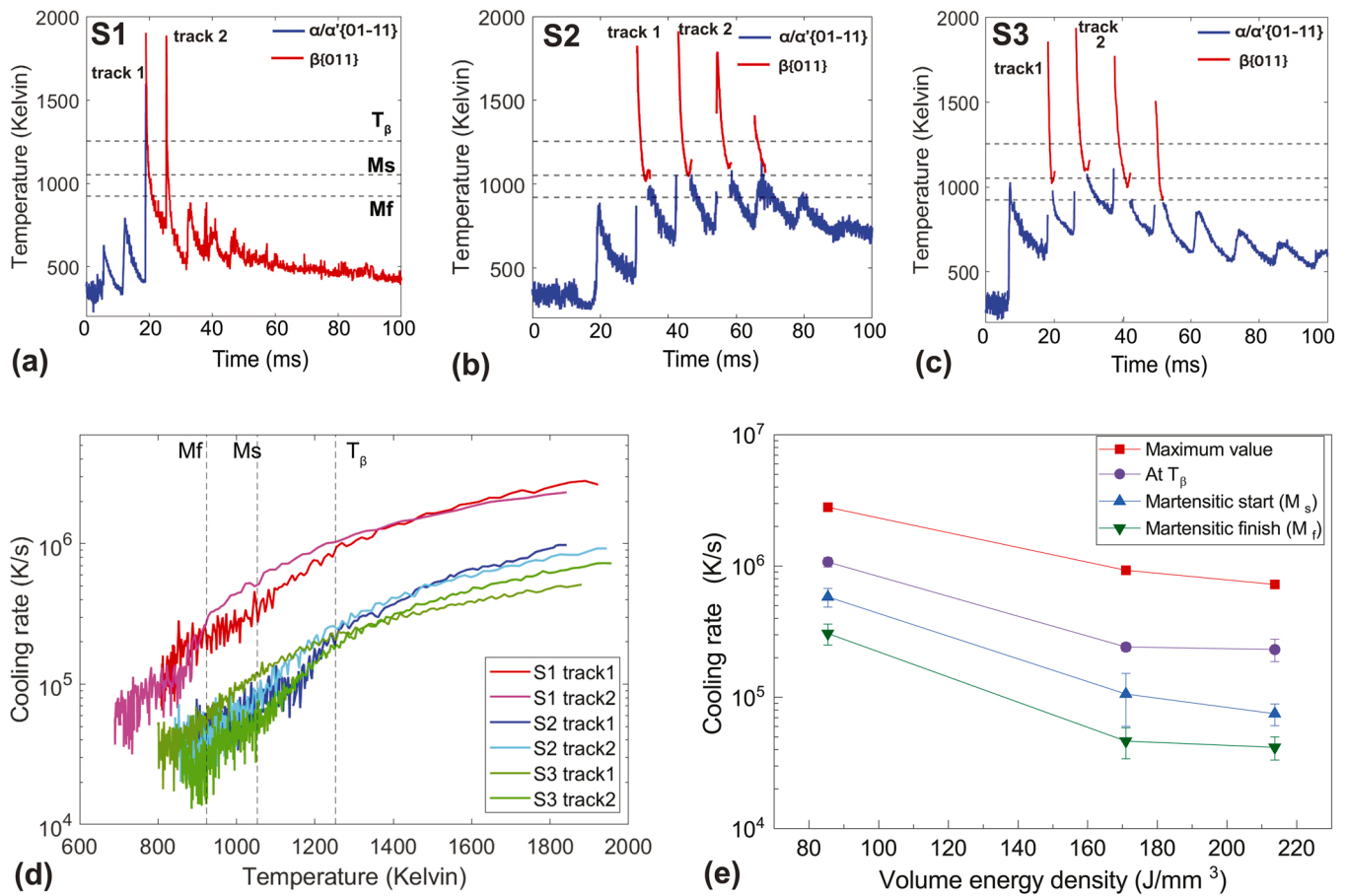


Fig. 3. (a–c) Temperatures profiles as a function of time calculated from $\{011\}\beta$ – red and $\{01.1\}\alpha/\alpha'$ – blue for three specimens. (d) The cooling rates as a function of temperature are calculated from the individual track labeled in (a–c). (e) The average cooling rates as a function of volume energy density at the maximum temperatures, β transus (T_β) \sim 1252 K, martensitic start (M_s) \sim 1053 K and martensitic finish (M_f) \sim 923 K of Ti-6Al-4V [38,41] respectively.

presence of Fe during solidification of the melt [19,24]. Furthermore, the phase maps show that in sample S1 (Fig. 4e) the β phase is dominant with an area fraction of about 80%. In contrast, sample S2 exhibits only around 15 % of β phase (Fig. 4h). The EDS maps demonstrate that the Fe distribution is rather heterogeneous in sample S1 (Fig. 4f) but relatively homogeneous in sample S2 (Fig. 4i). This suggests a higher level of homogeneity of Fe distribution in specimens printed with high VED (171 J/mm³). In S1, the EDS point measurements show the β grains exhibit an above-average Fe concentration (≥ 3.8 wt%), whereas the α/α' -grains are nearly depleted from Fe. In sample S2 a similar trend can be observed. The difference in Fe concentration between the β and α/α' regions is smaller compared to the case of S1. This result indicates a higher level of Fe homogeneity in as-built samples printed with larger energy inputs. The distributions of Ti, Al and V are quite homogenous in both samples, as shown in the Supplementary Materials Fig. S2. The distribution of Ti, V and Fe of S1–S3 were further characterized by XRF measurements over larger cross-sections (Supplementary Materials Fig. S3), confirming the EDS results.

3.3. Relationship between process parameters and mechanical properties

It is well known that the mechanical properties of additively manufactured Ti64 strongly depend on the phase fraction [45]. Tensile tests have been performed on samples S4 and S5. Fig. 5 shows the microstructures obtained by EBSD. Sample S4 exhibits a β phase fraction of 90 % (comparable to S1) whereas sample S5 exhibits an α/α' phase fraction of 70 % (comparable to S2). The laser process parameter for samples S1 and S4, and also for samples S2 and S5 are slightly different,

since the samples were processed in two different L-PBF systems. But the differences between the VED values are rather small (~ 4 – 9 J/mm³). This may result in minor changes in texture [46] and other microstructural parameters. Fig. 6 displays the mechanical response under tensile loading. Sample S4 reaches an ultimate tensile strength (UTS) of 1364 ± 59 MPa and a uniform elongation of 11.4 ± 1.9 %. Sample S5 exhibits a higher UTS of 1762 ± 50 MPa but lower ductility of 3.1 ± 0.6 %. In other words, sample S4 exhibit enhanced ductility and working hardening but relatively lower strength compared to sample S5.

4. Discussion

4.1. Factors that influence phase evolution

In conventional Ti64, the high-temperature β phase can be stabilized at room temperature for sufficiently low cooling rates. In literature, various critical cooling rates that suppress completely martensitic transformation to obtain the β phase have been reported. Ahmad and Rack found the β phase was retained below a critical cooling rate of 410 K/s [47], whereas Kenel et al. [48] and Oh et al. [9] observed the cooling rates for stabilization of the β phase that are one order of magnitude higher (~ 3000 K/s). By adding 3 wt% Fe to Ti64, the β metastable phase is partly stabilized at room temperature even for cooling rates as high as 10^6 K/s according to high-speed *operando* XRD (Fig. 2a and Fig. 3d). This indicates a significant role of in situ alloying on engineering phase fractions of as-built materials. Moreover, the results shown in Sections 3.1 and 3.2 reveal a significant impact of the laser process parameters on the in situ alloying process and resulting

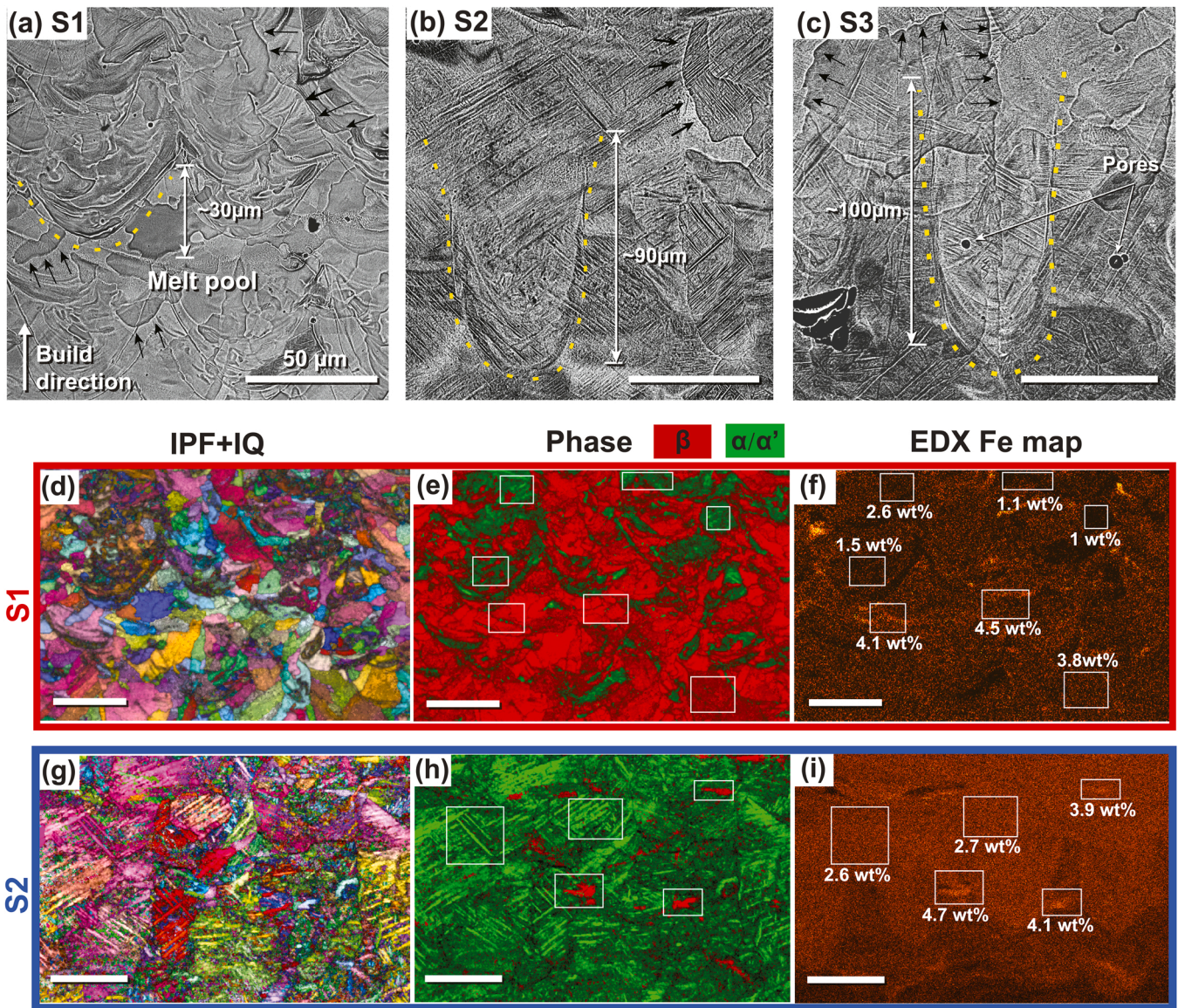


Fig. 4. Microstructures of the cross-sections of specimens printed with different laser parameters. (a–c) Back-scattered electron (BSE) micrographs showing different features after etching with Kroll's reagent. EBSD inverse pole figure (IPF) plus image quality (IQ) of S1 (d) and S2 (g). Phase map (α/α' is in green and β is in red) of the same regions in S1 (e) and S2 (h) respectively. EDS map of Fe distribution in S1 (f) and S2 (i). Scale bar, 50 μm .

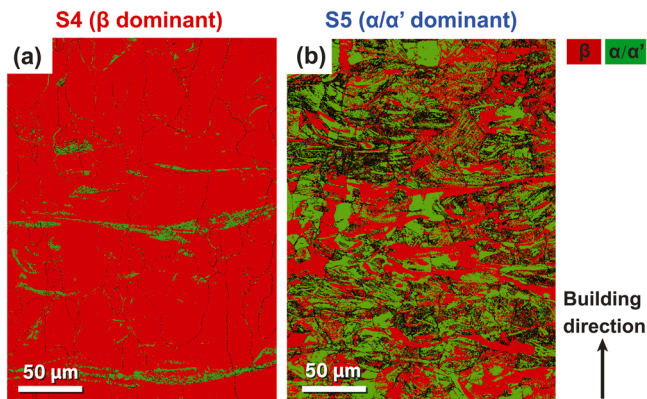


Fig. 5. Microstructures of the tensile specimens prior to deformation. Phase maps from electron backscatter diffraction (EBSD) measurements indicating β phase dominant (90 %) in S4 (b) and α/α' dominant (70 %) in S5 (d) respectively.

microstructures. In sample S1, printed with low VED, a large number of metastable β grains were stabilized at ambient temperature, in contrast to samples S2 and S3 fabricated with high VED. We have established the major contributing factors to this difference, namely the concentration and distribution of Fe.

It is reported that a minimum of 3.5 wt% Fe is needed to fully stabilize the β phase in Ti64-based alloys during water quenching [49,50]. To the authors' knowledge, no such lower limit of Fe concentration has been established for the high cooling rates that are observed during the L-PBF process. It is known that the chemical composition of a printed part can differ from the original composition of the powder feedstock due to the elemental loss during printing. Spatially resolved X-ray fluorescence (XRF) spectroscopy measurements have been conducted to investigate the chemical composition between samples S1–S3. The result shows that the Fe content in S1 is about 30–36 % higher than in S2 and S3 (Supplementary Materials Fig. S3). A similar result is also found in S4 and S5, where the Fe content is higher in the sample printed with lower VED (see also EDS measurements shown in Supplementary Materials Section 4). It is well known that vaporization increases with increasing

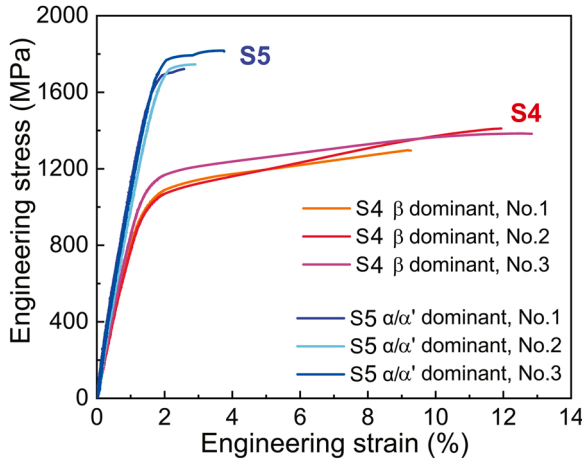


Fig. 6. Mechanical properties of as-built specimens printed with different laser parameters. Tensile stress-strain curves of β -dominant (S4) and α/α' -dominant (S5).

energy density. Furthermore, the evaporation rate of Fe is expected to be significantly larger compared to that of Ti due to the relatively lower boiling point (~ 425 K lower) [51]. In addition, the Fe particles with much finer sizes than Ti64 particles (Fig. 1c) are easier to evaporate or ejected by vapor-driven entrainment. The concentrations of Al and V in S1–S3 are quite similar according to the signal ratios from XRF measurements. The EDS measurements in S4 and S5 (Supplementary Materials Section 4) show ~ 6 wt% of Al and ~ 4 wt% of V, indicating negligible evaporation. This is probably due to the pre-alloying of Al and V in large Ti64 particles that alleviate preferential element loss deriving from size effects of the feedstock.

A second factor that plays a major role is the spatial distribution of the β stabilizers. Figs. 4f and 4i show that in samples S2 and S3 Fe is distributed more homogeneously as compared to sample S1. This is further confirmed by the XRF results shown in Supplementary Materials Fig. S3. In all samples, the Fe concentration in the β grains is significantly higher as compared to the α/α' grains. Interestingly, the Fe concentration in α/α' grains of sample S2 is higher compared to α/α' grains in sample S1 (Fig. 4). The Fe spreading during printing occurs via convection flow and diffusion. Both processes are highly dependent on the laser parameters and resulting thermal profiles. The *operando* X-ray diffraction experiments shown in Fig. 3 indicate that for sample S1 a given location on the top layer exhibits 1–2 short melting events, caused by the overlap between neighboring tracks, and the corresponding formation of the β phase. In samples S2 and S3, the melt pool and surrounding heat-affected zone are significantly larger. Here, the material experiences 4 subsequent phase transformations and an overall higher temperature for a similar time interval.

Inside the melt pool, the convection of liquid metals is primarily driven by the Marangoni flow, where Fe is mechanically mixed with Ti64 [52,53]. Here, we need to distinguish between conduction and keyhole modes, as schematically shown in Fig. 7. In the keyhole mode, the material undergoes significantly more melting-solidification cycles

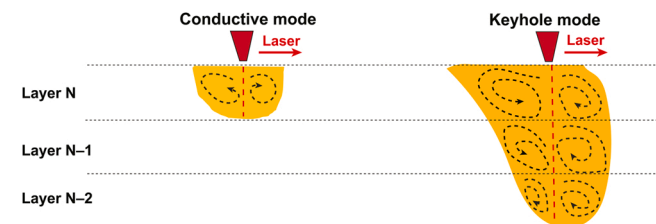


Fig. 7. Sketch of the Marangoni flow in melt pools for the conductive and keyhole modes.

because of the deeper melt pool. For instance, layer N-2 is remelted again during the depositing of layer N, as demonstrated in Fig. 7. These thermal cycles cause repetitive mixing inside the melt pool, effectively homogenizing the Fe distribution [54].

To evaluate the contribution of Fe diffusion during in situ alloying quantitatively, the diffusion length, X , in both liquid and solid states can be estimated by the following equation [55,56]:

$$X = \sqrt{6Dt} \quad (1)$$

where D is the diffusion coefficient of Fe in Ti and t is the diffusion time. As a boundary condition to solve the partial differential equation of Fick's second law the diffusion front of Fe in Ti64 is fixed at 1 %. In liquid Ti, the diffusion coefficient of Fe, $D_{Fe,Ti}$, can be calculated as [53, 57]:

$$D_{Fe,Ti} = \frac{0.002628 \sqrt{T^3 \cdot (m_{Fe} + m_{Ti}) / (2 \cdot m_{Fe} \cdot m_{Ti})}}{P \cdot \bar{d}^2 \cdot (\Omega_{Fe,Ti} \cdot T_{Fe,Ti})} \quad (2)$$

where P is atmosphere pressure, \bar{d} is the average atomic diameters of Fe and Ti atoms as 136 pm, $\Omega_{Fe,Ti} \cdot T_{Fe,Ti}$ is the collision integral as unity for rigid spheres, m_{Fe} and m_{Ti} are the atomic masses of Fe and Ti respectively and T is the temperature of the melt pool. According to experimental measurements with a high-speed infrared camera [58] and three-dimensional finite element modeling [59], the melt pool temperatures are in a range of 1933 K and 3300 K, i.e. between melting and boiling points of Ti64. Therefore the calculations are performed for the lower and upper limits and an average value, i.e. $T = 1933$ K, 2616 K and 3300 K. $D_{Fe,Ti}$ is computed as 3.25×10^{-8} m²/s. According to high-speed XRD measurements (Fig. 3a–c), the molten state lasted for 3×10^{-4} , 1.5×10^{-3} and 2.0×10^{-3} sec in S1–S3 respectively. Based on these numbers and assumptions, the diffusion lengths of Fe in liquid Ti (X_{liquid}) are listed in Table 2 for samples S1–S3.

After solidification, the Fe diffusion continues in both β and α/α' phases during cooling until [30]. The temperature-dependent diffusion coefficient in the solid state, D_{solid} , is calculated by the following equation expressed in the Arrhenius form for both β and α' phases until ambient temperature individually [60,61]:

$$D_{solid}(T) = D_0 \cdot \exp\left(-\frac{Q}{kT}\right) \quad (3)$$

where D_0 is pre-exponent coefficient [m²/s], Q is the activation energy for diffusion and k is Boltzmann's constant. Since the temperature as a function of time (Fig. 3a–c) is calculated from the *operando* XRD measurements, the $D_{solid}(T)$ can be determined as a function of time for each specimen. The diffusion length X at solid state (X_{solid}) is obtained by integrating an area below the curve, as listed in Table 2. The results show, as expected, that the diffusion in the liquid state is more pronounced than in the solid state. After solidification, the magnitude of Fe diffusion length is of the order of only a few micrometers. Therefore, it is expected that the effect of local chemical fluctuation on temperatures calculated from the X-ray illuminated region ($45 \times 46 \mu\text{m}^2$) after solidification should be rather limited. In addition, thermal diffusion driven by steep temperature gradients (~ 0.1 – 1 K/ μm) [62] at the adjacent heat-affected zone (HAZ) further facilitates in situ alloying. It has been reported that this can result in nanometer-sized clusters due to the extremely short processing time (\sim ms) during L-PBF [63]. The magnitude of the diffusion length (X_{total}) is of an order of tens of

Table 2
Diffusion length of β -stabilizer Fe in liquid and solid titanium.

Specimen number	X_{liquid} (μm)	X_{solid} (μm)
S1	7.0 ± 1.1	1.0 ± 0.2
S2	15.5 ± 2.4	4.1 ± 0.6
S3	17.8 ± 2.8	6.6 ± 0.9

microns, which is not sufficient to induce the present level of Fe homogeneity in as-built structures (Figs. 4f and 4i). It should be noted that these calculations apply to the upper layer only. In the layers below, additional thermal cycling during printing will lead to further diffusion of Fe. Hence, the present Fe homogeneity indicates the more significant role of convection flow to mix Fe with Ti64 melts inside the melt pool. In 304 L stainless steel printed with elemental powders, higher level of chemical homogeneity was achieved in samples produced with larger volume energy densities according to Aota et al. [64]. This phenomenon is also reported in Fe-Ni alloys as well [65]. Higher energy inputs induce longer molten state (0.3 μ s, 1.5 μ s and 2.0 μ s in S1–S3 respectively) inside the melt pool, which promotes the mixing to homogenize Fe distribution. This alleviates the local enrichment of Fe and influences the phase stability of β -Ti to decrease β phase fraction in S2 and S3.

By varying laser parameters from conduction mode to keyhole mode, the microstructures of as-built Ti alloys can be effectively engineered. Previously, the chemical compositions have been considered to play the main role in in situ alloying process and microstructures formation [24, 29,53]. Here, we reveal the significant effect of laser parameters on elemental distribution and resulting microstructures.

4.2. Correlation between microstructure and mechanical properties

By varying the process parameters, both the strength and ductility of Ti643 can be altered significantly. Two representative microstructures, i.e. β (S4) or α/α' (S5) phase dominant, are chosen for tensile testing to reveal their significant impacts on the mechanical properties of printed Ti alloys. It should be noted that small differences among the microstructures of the samples with low VED (S1–S4) and among the samples with high VED (S2–S5) exist (Figs. 4 and 5), which may impact their mechanical properties. However, it is reasonable to assume that the effect will be much smaller compared to the difference between the low and high VED samples. Fig. 8 compares the ultimate tensile strength of the presented quaternary Ti643 alloy with an alloy created from a blend of Ti64 and 316L [29] and with Ti64 alloys fabricated by various AM techniques: L-PBF [11,13,21,66–68], E-PBF [66,69–71] and DED [3, 72–74]. Ti643 exhibits superior properties as a synergy of high strength and enhanced ductility in the as-built state without any post-processing treatments. Sample S4 with a large fraction of β phase exhibits simultaneously enhanced strength and ductility. Sample S5 with dominant martensitic phase exhibits very high strength, albeit at the expense of ductility. The high strength in present quaternary Ti643 alloys is partially ascribed to the solid solution strengthening of Fe in the β or α' phase. In addition, precipitates of fine α' and ω phases in metastable β

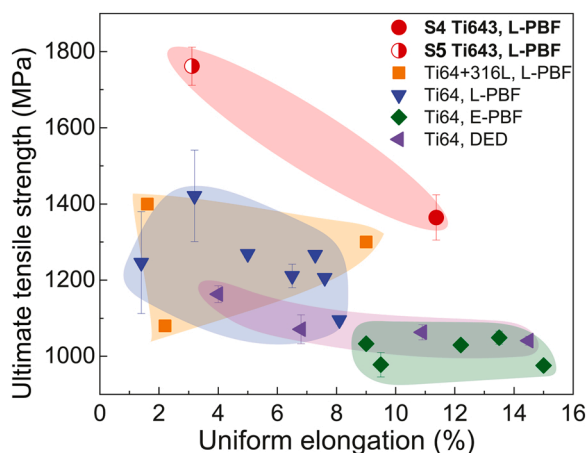


Fig. 8. Ultimate tensile strength versus uniform elongation of as-built Ti643 compared with Ti64 mixed with 316L powder [29] and Ti64 produced by different AM techniques: L-PBF [11,13,21,66–68], E-PBF [66,69–71] and DED [3,72–74].

grains induced by rapid cooling in L-PBF process might also contribute to the strengthening [26]. Further studies on the presence of ω phases in samples produced using different process parameters is on-going. Such precipitate strengthening was observed in Ti-10V-2Fe-3Al alloys with the same alloying elements after water quenching [75]. The enhanced ductility in S4 is probably attributed to a combination of inherent ductility of the β phase and the strain-induced transformation from retained metastable β phase to martensite, i.e. the TRIP effect during deformation in metastable β -Ti alloys [29,50]. The notable work hardening observed in S4 is associated with the phase hardening of α/α' in relative softer β grains. This phenomenon has been also reported in Fe modified Ti64 alloys [16,76]. Nevertheless, the uniform elongation ($\sim 11.4\%$) and work hardening achieved in S4 are still relatively inferior to typical TRIP β -Ti alloys with complete metastable β phase structures and much higher contents of β -stabilizers [77]. These findings demonstrate that the mechanical properties of L-PBF processed Ti-Al-V-Fe alloy could be further enhanced via tuning chemical compositions and microstructures. The details of plastic deformation in Ti643 specimens are beyond the scope of the present paper and are subject of an on-going investigation.

5. Conclusion

In the present study, we have demonstrated an effective method to engineer microstructures of additively manufactured Ti6Al4V-Fe alloys by varying laser parameters during the L-PBF process using blended powders. High-speed *operando* X-ray diffraction has been performed during printing to measure phase evolution and thermal profiles. The temperatures as a function of time are used to calculate cooling rates and diffusion lengths, revealing the effective role of Fe addition on the stabilization of metastable β phase under rapid cooling conditions. The microstructures of the specimens are investigated to show the effect of energy input on the elemental distribution and phase fractions. Finally, the mechanical properties of representative samples were tested. The following conclusions can be drawn:

- The metastable β -Ti phase can be stabilized to ambient temperatures under rapid cooling ($\sim 5.8 \times 10^5$ – 1.1×10^6 K/s) during the L-PBF process using blended powders consisting of Ti-6Al-4V mixed with 3 wt% Fe particles.
- Samples printed with higher energy density experience stronger thermal cycling, i.e. more cycles exhibit peak temperatures higher than the β transus temperature, compared to the samples printed with low energy density.
- The as-built microstructures can be varied from β dominant to almost complete α' by increasing the energy input. This can be ascribed to the density and distribution of Fe, which in turn, is linked to process parameters. At low energy density Fe is distributed heterogeneously in the microstructure. In contrast, high energy density leads to more Fe loss and better homogeneous mixing of Fe atoms in the Ti64 matrix, which results in a significantly lower stabilized β -fraction after printing.
- The printed microstructures that contain a large β fraction achieve simultaneously a high strength and ductility. The strength is higher when the α' phase is dominant, but its ductility has deteriorated.

This work exhibits a paradigm to engineer microstructures of additively manufactured Ti alloys. It enables to manufacture specific microstructures and paves the way to create functionally gradient properties for designed properties. It is anticipated this strategy can be further adopted by various alloy systems for L-PBF manufacturing via powders composition design and processing parameters control.

CRedit authorship contribution statement

Steven Van Petegem: Writing – review & editing, Visualization,

Supervision, Software, Methodology, Investigation, Formal analysis, Conceptualization. **Ming Chen**: Writing – original draft, Visualization, Software, Investigation, Formal analysis, Conceptualization. **Marco Simonelli**: Writing – review & editing, Validation, Resources, Funding acquisition, Conceptualization. **Zhiyi Zhou**: Writing – review & editing, Validation, Investigation, Formal analysis. **Yau Yau Tse**: Resources, Formal analysis. **Malgorzata Makowska**: Investigation. **Cynthia Chang**: Investigation. **Helena Van Swygenhoven**: Writing – review & editing, Supervision, Project administration, Methodology, Funding acquisition, Conceptualization. **Dario Ferreira Sanchez**: Resources, Methodology, Investigation.

Declaration of Competing Interest

The authors declare that they have no known competing financial interests or personal relationships that could have appeared to influence the work reported in this paper.

Data Availability

Data will be made available on request.

Acknowledgement

We would like to thank K. Kunze and L. Grafuha Morales (ScopeM, ETH Zurich) for their help in the sample characterization with SEM and D. Grolimund for the XRF measurements and analysis. MS and YYT acknowledge the use of facilities within the Loughborough Materials Characterization Centre and for access to the Helios PFIB, funded by the EPSRC Grant EP/P030599/1. MC and HVS are grateful for the financial support of Additive Manufacturing of Precious metals Alloys (PRE-AMPA) project, funded by the ETH Board and the Swiss Watch and Precious Metals Industry.

Appendix A. Supporting information

Supplementary data associated with this article can be found in the online version at [doi:10.1016/j.addma.2022.103173](https://doi.org/10.1016/j.addma.2022.103173).

References

- [1] L. Thijs, F. Verhaeghe, T. Craeghs, J. Van Humbeeck, J.P. Kruth, A study of the microstructural evolution during selective laser melting of Ti-6Al-4V, *Acta Mater.* 58 (2010) 3303–3312.
- [2] M. Simonelli, Y.Y. Tse, C. Tuck, Effect of the build orientation on the mechanical properties and fracture modes of SLM Ti-6Al-4V, *Mater. Sci. Eng. A* 616 (2014) 1–11.
- [3] J. Alcisto, A. Enriquez, H. Garcia, S. Hinkson, T. Steelman, E. Silverman, P. Valdovino, H. Gigerenzer, J. Foyos, J. Ogren, J. Dorey, K. Karg, T. McDonald, O. S. Es-Said, Tensile properties and microstructures of laser-formed Ti-6Al-4V, *J. Mater. Eng. Perform.* 20 (2011) 203–212.
- [4] S. Leuders, M. Thöne, A. Riemer, T. Niendorf, T. Tröster, H.A. Richard, H.J. Maier, On the mechanical behaviour of titanium alloy TiAl6V4 manufactured by selective laser melting: fatigue resistance and crack growth performance, *Int. J. Fatigue* 48 (2013) 300–307.
- [5] S. Liu, Y.C. Shin, Additive manufacturing of Ti6Al4V alloy: a review, *Mater. Des.* 164 (2019), 107552.
- [6] L. Qian, J. Mei, J. Liang, X. Wu, Influence of position and laser power on thermal history and microstructure of direct laser fabricated Ti-6Al-4V samples, *Mater. Sci. Technol.* 21 (2005) 597–605.
- [7] M. Simonelli, Y.Y. Tse, C. Tuck, The formation of $\alpha + \beta$ microstructure in as-fabricated selective laser melting of Ti-6Al-4V, *J. Mater. Res.* 29 (2014) 2028–2035.
- [8] A. Zafari, M.R. Barati, K. Xia, Controlling martensitic decomposition during selective laser melting to achieve best ductility in high strength Ti-6Al-4V, *Mater. Sci. Eng. A* 744 (2019) 445–455.
- [9] S.A. Oh, R.E. Lim, J.W. Aroh, A.C. Chuang, B.J. Gould, B. Amin-Ahmadi, J. Bernier, T. Sun, P.C. Pistorius, R.M. Suter, A.D. Rollett, High speed synchrotron X-ray diffraction experiments resolve microstructure and phase transformation in laser processed Ti-6Al-4V, *Mater. Res. Lett.* 9 (2021) 429–436.
- [10] J. Haubrich, J. Gussone, P. Barriobero-Vila, P. Kürsteiner, E.A. Jäggle, D. Raabe, N. Schell, G. Requena, The role of lattice defects, element partitioning and intrinsic heat effects on the microstructure in selective laser melted Ti-6Al-4V, *Acta Mater.* 167 (2019) 136–148.
- [11] T. Vilaro, C. Colin, J.D. Bartout, As-fabricated and heat-treated microstructures of the Ti-6Al-4V alloy processed by selective laser melting, *Metall. Mater. Trans. A* 42 (2011) 3190–3199.
- [12] C. de Formanoir, A. Brulard, S. Vivès, G. Martin, F. Prima, S. Michotte, E. Rivière, A. Dolimont, S. Godet, A strategy to improve the work-hardening behavior of Ti-6Al-4V parts produced by additive manufacturing, *Mater. Res. Lett.* 5 (2017) 201–208.
- [13] B. Vrancken, L. Thijs, J.-P. Kruth, J. Van Humbeeck, Heat treatment of Ti6Al4V produced by selective laser melting: microstructure and mechanical properties, *J. Alloy. Compd.* 541 (2012) 177–185.
- [14] T. Hua, C. Jing, Z. Fengying, L. Xin, H. Weidong, Microstructure and mechanical properties of laser solid formed Ti-6Al-4V from blended elemental powders, *Rare Met. Mater. Eng.* 38 (2009) 574–578.
- [15] A. Zafari, K. Xia, Superior titanium from hybridised microstructures – a new strategy for future alloys, *Scr. Mater.* 173 (2019) 61–65.
- [16] F. Huber, T. Papke, C. Scheitler, L. Hanrieder, M. Merklein, M. Schmidt, In situ formation of a metastable β -Ti alloy by laser powder bed fusion (L-PBF) of vanadium and iron modified Ti-6Al-4V, *Metals* 8 (2018) 1067.
- [17] S.L. Sing, S. Huang, G.D. Goh, G.L. Goh, C.F. Tey, J.H.K. Tan, W.Y. Yeong, Emerging metallic systems for additive manufacturing: in-situ alloying and multi-metal processing in laser powder bed fusion, *Prog. Mater. Sci.* 119 (2021), 100795.
- [18] M.H. Mosallanejad, B. Niroomand, A. Aversa, A. Saboori, In-situ alloying in laser-based additive manufacturing processes: a critical review, *J. Alloy. Compd.* 872 (2021), 159567.
- [19] H. Azizi, H. Zurob, B. Bose, S. Reza Ghiaasiaan, X. Wang, S. Coulson, V. Duz, A. B. Phillion, Additive manufacturing of a novel Ti-Al-V-Fe alloy using selective laser melting, *Addit. Manuf.* 21 (2018) 529–535.
- [20] S. Huang, P. Kumar, W.Y. Yeong, R.L. Narayan, U. Ramamurty, Fracture behavior of laser powder bed fusion fabricated Ti41Nb via in-situ alloying, *Acta Mater.* 225 (2022), 117593.
- [21] B. Vrancken, L. Thijs, J.P. Kruth, J. Van Humbeeck, Microstructure and mechanical properties of a novel β titanium metallic composite by selective laser melting, *Acta Mater.* 68 (2014) 150–158.
- [22] A.M. Vilardell, I. Yadroitsev, I. Yadroitsava, M. Albu, N. Takata, M. Kobashi, P. Krakhmalev, D. Kouprianoff, G. Kothleitner, A. du Plessis, Manufacturing and characterization of in-situ alloyed Ti6Al4V(ELI)-3 at% Cu by laser powder bed fusion, *Addit. Manuf.* 36 (2020), 101436.
- [23] D. Kuroda, M. Niinomi, M. Morinaga, Y. Kato, T. Yashiro, Design and mechanical properties of new β type titanium alloys for implant materials, *Mater. Sci. Eng. A* 243 (1998) 244–249.
- [24] M. Simonelli, D.G. McCartney, P. Barriobero-Vila, N.T. Aboulkhair, Y.Y. Tse, A. Clare, R. Hague, The influence of iron in minimizing the microstructural anisotropy of Ti-6Al-4V produced by laser powder-bed fusion, *Metall. Mater. Trans. A Phys. Metall. Mater. Sci.* 51 (2020) 2444–2459.
- [25] T.C. Dzugbewu, I. Yadroitsev, P. Krakhmalev, I. Yadroitsava, A. Du Plessis, Optimal process parameters for in-situ alloyed Ti15Mo structures by direct metal laser sintering, in: *Proceedings of the SSF 2017-The 28th Annu. Int. Solid Free. Fabr. Symp. Austin, August 7–9, 2017, Univ. Texas, 2017*, pp. 75–96.
- [26] H. Azizi, H. Zurob, B. Bose, S. Reza Ghiaasiaan, X. Wang, S. Coulson, V. Duz, A. B. Phillion, Additive manufacturing of a novel Ti-Al-V-Fe alloy using selective laser melting, *Addit. Manuf.* 21 (2018) 529–535.
- [27] B.A. Welk, N. Taylor, Z. Kloenne, K.J. Chaput, S. Fox, H.L. Fraser, Use of alloying to effect an equiaxed microstructure in additive manufacturing and subsequent heat treatment of high-strength titanium alloys, *Metall. Mater. Trans. A* 52 (2021) 5367–5380.
- [28] X. Wang, L.-J. Zhang, J. Ning, Sen Li, L.-L. Zhang, J. Long, W. Ma, Fe element promotes the transformation from columnar to equiaxed grains and the formation of ultrafine microstructure of Ti-6Al-4V alloy by laser wire deposition, *Addit. Manuf.* 48 (2021), 102442.
- [29] T. Zhang, Z. Huang, T. Yang, H. Kong, J. Luan, A. Wang, D. Wang, W. Kuo, Y. Wang, C.-T. Liu, In situ design of advanced titanium alloy with concentration modulations by additive manufacturing, *Science* (80-) 374 (2021) 478–482.
- [30] F.F. Ahmed, S.J. Clark, C.L. Alex Leung, L. Stanger, J. Willmott, S. Marussi, V. Honkimaki, N. Haynes, H.S. Zurob, P.D. Lee, A.B. Phillion, Achieving homogeneity in a high-Fe β -Ti alloy laser-printed from blended elemental powders, *Mater. Des.* 210 (2021), 110072.
- [31] T. Nagase, T. Hori, M. Todai, S.H. Sun, T. Nakano, Additive manufacturing of dense components in beta-titanium alloys with crystallographic texture from a mixture of pure metallic element powders, *Mater. Des.* 173 (2019), 107771.
- [32] I.A. Polozov, E. Borisov, V. Popovich, Effect of selective laser melting process parameters and heat treatment on microstructure and properties of titanium alloys produced from elemental powders, *Key Eng. Mater.* 822 (2019) 549–555.
- [33] S. Hocine, S. Van Petegem, U. Frommherz, G. Tinti, N. Casati, D. Grolimund, H. Van Swygenhoven, A miniaturized selective laser melting device for operando X-ray diffraction studies, *Addit. Manuf.* 34 (2020), 101194.
- [34] S. Hocine, H. Van Swygenhoven, S. Van Petegem, C.S.T. Chang, T. Maimaitiyili, G. Tinti, D. Ferreira Sanchez, D. Grolimund, N. Casati, Operando X-ray diffraction during laser 3D printing, *Mater. Today* 34 (2020) 30–40.
- [35] G. Tinti, A. Bergamaschi, S. Cartier, R. Dinapoli, D. Greiffenberg, I. Johnson, J. H. Jungmann-Smith, D. Mezza, A. Mozzanica, B. Schmitt, X. Shi, Performance of the EIGER single photon counting detector, *J. Instrum.* 10 (2015), C03011.
- [36] G. Ashiotis, A. Deschilde, Z. Nawaz, J.P. Wright, D. Karkoulis, F.E. Picca, J. Kieffer, The fast azimuthal integration Python library: pyFAI, *J. Appl. Crystallogr.* 48 (2015) 510–519.

- [37] Y.S. Touloukian, R.K. Kirby, R.E. Taylor, P.D. Desai, *Thermal Expansion*, Springer, US, Boston, MA, 1975.
- [38] A. Ducato, L. Fratini, M. La Cascia, G. Mazzola, An automated visual inspection system for the classification of the phases of Ti-6Al-4V titanium alloy, in: R. Wilson, E. Hancock, A. Bors, W. Smith (Eds.), *Comput. Anal. Images Patterns*, Springer Berlin Heidelberg, Berlin, Heidelberg, 2013, pp. 362–9.
- [39] I. Polmear, D. StJohn, J.-F. Nie, M. Qian, *The Light Metals*, in: *Light Alloy*, Elsevier, 2017, pp. 1–29.
- [40] S. Neelakantan, P.E.J. Rivera-Díaz-del-Castillo, S. van der Zwaag, Prediction of the martensite start temperature for β titanium alloys as a function of composition, *Scr. Mater.* 60 (2009) 611–614.
- [41] S.L. Lu, M. Qian, H.P. Tang, M. Yan, J. Wang, D.H. StJohn, Massive transformation in Ti-6Al-4V additively manufactured by selective electron beam melting, *Acta Mater.* 104 (2016) 303–311.
- [42] M. Chen, M. Simonelli, S. Van Petegem, Y.Y. Tse, C.S.T. Chang, M. Grazyna, D. Ferreira, H. Van Swygenhoven, A quantitative study of thermal cycling along the build direction of Ti-6Al-4V produced by laser powder bed fusion 2022, n.d., (in preparation).
- [43] E. Lee, R. Banerjee, S. Kar, D. Bhattacharyya, H.L. Fraser, Selection of α variants during microstructural evolution in α/β titanium alloys, *Philos. Mag.* 87 (2007) 3615–3627.
- [44] C. Zhao, N.D. Parab, X. Li, K. Fezzaa, W. Tan, A.D. Rollett, T. Sun, Critical instability at moving keyhole tip generates porosity in laser melting, *Science* (80-) 370 (2020) 1080–1086.
- [45] H. Galarraga, R.J. Warren, D.A. Lados, R.R. Dehoff, M.M. Kirka, P. Nandwana, Effects of heat treatments on microstructure and properties of Ti-6Al-4V ELI alloy fabricated by electron beam melting (EBM), *Mater. Sci. Eng. A* 685 (2017) 417–428.
- [46] C.M. Cepeda-Jiménez, F. Potenza, E. Magalini, V. Luchin, A. Molinari, M.T. Pérez-Prado, Effect of energy density on the microstructure and texture evolution of Ti-6Al-4V manufactured by laser powder bed fusion, *Mater. Charact.* 163 (2020), 110238.
- [47] T. Ahmed, H.J. Rack, Phase transformations during cooling in $\alpha + \beta$ titanium alloys, *Mater. Sci. Eng. A* 243 (1998) 206–211.
- [48] C. Kenel, D. Grolimund, X. Li, E. Panepucci, V.A. Samson, D.F. Sanchez, F. Marone, C. Leinenbach, In situ investigation of phase transformations in Ti-6Al-4V under additive manufacturing conditions combining laser melting and high-speed micro-X-ray diffraction, *Sci. Rep.* 7 (2017) 1–10.
- [49] P.J. Bania, Beta titanium alloys and their role in the titanium industry, *JOM* 46 (1994) 16–19.
- [50] C. Hammond, J. Nutting, The physical metallurgy of superalloys and titanium alloys, *Met. Sci.* 11 (1977) 474–490.
- [51] J. Liu, P. Wen, Metal vaporization and its influence during laser powder bed fusion process, *Mater. Des.* 215 (2022), 110505.
- [52] S.J. Clark, C.L.A. Leung, Y. Chen, L. Sinclair, S. Marussi, P.D. Lee, Capturing Marangoni flow via synchrotron imaging of selective laser melting, *IOP Conf. Ser. Mater. Sci. Eng.* 861 (2020), 012010.
- [53] A. Zafari, E.W. Lui, S. Jin, M. Li, T.T. Molla, G. Sha, K. Xia, Hybridisation of microstructures from three classes of titanium alloys, *Mater. Sci. Eng. A* 788 (2020), 139572.
- [54] C.H. Ng, M.J. Bermingham, M.S. Dargusch, Eliminating segregation defects during additive manufacturing of high strength β -titanium alloys, *Addit. Manuf.* 39 (2021), 101855.
- [55] G. Gottstein, *Physical Foundations of Materials Science*, Springer Berlin Heidelberg, Berlin, Heidelberg, 2004.
- [56] A.M. Berezhevskii, G. Sutmann, Time and length scales for diffusion in liquids, *Phys. Rev. E* 65 (2002), 060201.
- [57] J.O. Hirschfelder, C.F. Curtiss, R.B. Bird, *Molecular theory of gases and liquids*, *Mol. Theory Gases Liq.* (1964).
- [58] P.A. Hooper, Melt pool temperature and cooling rates in laser powder bed fusion, *Addit. Manuf.* 22 (2018) 548–559.
- [59] K. Karayagiz, A. Elwany, G. Tapia, B. Franco, L. Johnson, J. Ma, I. Karaman, R. Arroyave, Numerical and experimental analysis of heat distribution in the laser powder bed fusion of Ti-6Al-4V, *IJSE Trans.* 51 (2019) 136–152.
- [60] H. Nakajima, M. Koiwa, Diffusion in titanium, *ISIJ Int.* 31 (1991) 757–766.
- [61] R.A. Perez, H. Nakajima, F. Dymant, Diffusion in α Ti and Zr, *Mater. Trans.* 44 (2003) 2–13.
- [62] C.H. Fu, Y.B. Guo, Three-dimensional temperature gradient mechanism in selective laser melting of Ti-6Al-4V, *J. Manuf. Sci. Eng. Trans. ASME* 136 (2014) 1–7.
- [63] M.V. Pantawane, S. Dasari, S.A. Mantri, R. Banerjee, N.B. Dahotre, Rapid thermokinetics driven nanoscale vanadium clustering within martensite laths in laser powder bed fused additively manufactured Ti6Al4V, *Mater. Res. Lett.* 8 (2020) 383–389.
- [64] L. Shoji Aota, P. Bajaj, H.R. Zschommler Sandim, E. Aimé Jägler, Laser powder-bed fusion as an alloy development tool: parameter selection for in-situ alloying using elemental powders, *Materials* 13 (2020) 3922.
- [65] J.T. Strauss, M.J. Stucky, Laser additive manufacturing processing of a mixture of iron and nickel powders, in: *Solid Free. Fabr. 2016 Proc. 27th Annu. Int. Solid Free. Fabr. Symp. - An Addit. Manuf. Conf. SFF 2016*, 2016, pp. 426–37.
- [66] B. Wysocki, P. Maj, R. Sitek, J. Buhagiar, K. Kurzydowski, W. Świączkowski, Laser and electron beam additive manufacturing methods of fabricating titanium bone implants, *Appl. Sci.* 7 (2017) 657.
- [67] D.A. Hollander, M. von Walter, T. Wirtz, R. Sellei, B. Schmidt-Rohlfing, O. Paar, H.-J. Erli, Structural, mechanical and in vitro characterization of individually structured Ti-6Al-4V produced by direct laser forming, *Biomaterials* 27 (2006) 955–963.
- [68] L. Facchini, E. Magalini, P. Robotti, A. Molinari, S. Höges, K. Wissenbach, Ductility of a Ti-6Al-4V alloy produced by selective laser melting of prealloyed powders, *Rapid Prototyp. J.* 16 (2010) 450–459.
- [69] Y. Zhai, H. Galarraga, D.A. Lados, Microstructure, static properties, and fatigue crack growth mechanisms in Ti-6Al-4V fabricated by additive manufacturing: LENS and EBM, *Eng. Fail. Anal.* 69 (2016) 3–14.
- [70] H.K. Rafi, N.V. Karthik, H. Gong, T.L. Starr, B.E. Stucker, Microstructures and mechanical properties of Ti6Al4V parts fabricated by selective laser melting and electron beam melting, *J. Mater. Eng. Perform.* 22 (2013) 3872–3883.
- [71] N. Hrabec, T. Quinn, Effects of processing on microstructure and mechanical properties of a titanium alloy (Ti-6Al-4V) fabricated using electron beam melting (EBM), Part 2: energy input, orientation, and location, *Mater. Sci. Eng. A* 573 (2013) 271–277.
- [72] M. Seifi, A. Salem, J. Beuth, O. Harrysson, J.J. Lewandowski, Overview of materials qualification needs for metal additive manufacturing, *JOM* 68 (2016) 747–764.
- [73] B.E. Carroll, T.A. Palmer, A.M. Beese, Anisotropic tensile behavior of Ti-6Al-4V components fabricated with directed energy deposition additive manufacturing, *Acta Mater.* 87 (2015) 309–320.
- [74] G.P. Dinda, L. Song, J. Mazumder, Fabrication of Ti-6Al-4V scaffolds by direct metal deposition, *Metall. Mater. Trans. A* 39 (2008) 2914–2922.
- [75] J.D. Cotton, R.D. Briggs, R.R. Boyer, S. Tamirisakandala, P. Russo, N. Shchetnikov, J.C. Fanning, State of the art in beta titanium alloys for airframe applications, *JOM* 67 (2015) 1281–1303.
- [76] M.L. Meier, D.R. Lesuer, A.K. Mukherjee, The effects of the α/β phase proportion on the superplasticity of Ti-6Al-4V and iron-modified Ti-6Al-4V, *Mater. Sci. Eng. A* 154 (1992) 165–173.
- [77] G. Zhao, X. Li, N. Petrinic, Materials information and mechanical response of TRIP/TWIP Ti alloys, *Npj Comput. Mater.* 7 (2021) 91.